Evaporation-assisted magnetic separation of rare earth ions in aqueous solutions

Lei, Z.; Fritzsche, B.; Eckert, K.;

Evaporation-assisted magnetic separation of rare earth ions in aqueous solutions[†]

Zhe Lei,[*,‡,¶] Barbara Fritzsche,[‡] and Kerstin Eckert[*,‡,¶]

‡*Institute of Processing Engineering and Environmental Technology, Technische Universität Dresden, D-01069 Dresden, Germany*

¶*Institute of Fluid Dynamics, Helmholtz-Zentrum Dresden-Rossendorf (HZDR), D-01314 Dresden, Germany*

E-mail: Zhe.Lei@tu-dresden.de; Kerstin.Eckert@tu-dresden.de

Abstract

This work aims to answer the question of why an enrichment of paramagnetic ions can be observed in a magnetic field gradient despite the presence of a counteracting Brownian motion. For that purpose, we study a rare earth chloride ($DyCl_3$) solution in which weak evaporation is adjusted by means of small differences in the vapor pressure. The temporal evolution of the refractive index field of this solution, as a result of heat and mass transfer, is measured by means of a Mach-Zehnder interferometer. We develop a numerical algorithm which splits the refractive index field into two parts, one space-dependent and conservative and the other time-dependent and transient. By using this algorithm in conjunction with a numerical simulation of the temperature and concentration field, we are able to show that 90% of the refractive index in the evaporation-driven boundary layer is caused by an increase in the concentration of $Dy(III)$ ions. A simplified analysis of the gravitational and magnetic forces, entering

[†]

the Rayleigh number, leads to a diagram of the system's instability. Accordingly, the enrichment layer of elevated Dy(III) concentration is placed in a spatial zone dominated by a field gradient force. This leads to the unconditional stability of this layer in the present configuration. The underlying mechanism is the levitation and reshaping of the evaporation-driven boundary layer by the magnetic field gradient.

1 Introduction

The magnetic field gradient force,

$$\vec{f_m} = \frac{\chi_{mol}}{\mu_0}(\vec{B} \cdot \nabla)\vec{B} = \frac{\chi_{mol}}{2\mu_0}\nabla\vec{B}^2 \tag{1}$$

provided by an inhomogeneous magnetic field of induction $\vec{B}$ (μ_0: permeability of free space) is a versatile tool to separate ferro- and superparamagnetic components, possessing a magnetic susceptibilty χ. $\vec{f_m}$ has been commercially utilized for a long time in sorting scrap metal or in mineral processing to separate iron-bearing or paramagnetic ore particles.[1] The separable particle sizes extend over a wide range, starting from 10^{-2} m until about several 10^{-6} m, achieved in modern high-field-gradient magnetic separators (HGMS).[2] Acting on a comparable particle size, $\vec{f_m}$ is now also extensively used in bioengineering to capture biological material by means of functionalized magnetic microparticles in HGMS.[3–5]

The question of how to separate or manipulate even smaller objects, namely paramagnetic ions, by means of $\vec{f_m}$ has driven numerous research activities over the past two decades. In particular, $\vec{f_m}$ has been successfully applied in magnetoelectrochemistry, see recent review articles[6,7] together with Ref.[8] which explains the basics of the $\vec{f_m}$-driven mass transport in the electrolyte in the vicinity of small high-power NdFeB magnets. If the paramagnetic ions are the electroactive species in the electrochemical system, the electric current inside the electrolyte causes a concentration gradient of the paramagnetic ions at the cathode. As a result, the curl of $\vec{f_m}$, i.e. $\nabla \times \vec{f_m}$, becomes different from zero and a small-scale

convective flow appears.[9] This flow enhances mass transport, as shown recently at magnetic nanoparticle electrodes,[10] or assists the patterning of metallic deposits.[6,7,11,12]

However, even without an electric current, paramagnetic ions in an aqueous solution are reported to behave remarkably in the presence of $\vec{f}_m$.[13–21] Refs.[14] describes a confinement of the paramagnetic ions, produced by etching of a magnetized steel ball in an acid solution in areas of high magnetic flux density. While the shape of these zones could be explained qualitatively by the balance between hydrostatic and osmotic pressure, the large quantitative differences lead to the conclusion that $\vec{f}_m$ is too weak for the observed trapping of paramagnetic ions. In contrast to Ref.,[14] our previous works did not contain a local source of paramagnetic ions but started with an initially homogeneous aqueous solution of either a transition metal ion, $Mn(II)$,[13,15] or a rare earth ion, $Dy(III)$.[16] In both cases, an enrichment of these ions up to 2 % of the bulk concentration was found in the high field gradient zone of permanent magnets placed on top of the solution. A comparable enrichment of about 2% was measured by another group in Ref.[20] in a $HoCl_3$ solution, where a permanent magnet was applied at the bottom of the container. In Ref.[21] the magnetomigration of paramagnetic (Dy^{3+}, Gd^{3+}) and diamagnetic (Y^{3+}) rare earth ions was studied in a gel. A continuous concentration increase up to 10% at 5 T was found for paramagnetic ions in the region of higher field gradient force, while a decrease was measured for diamagnetic Y^{3+} ions.

Generally, the possibility to separate the rare earth ions magnetically, instead of via liquid-liquid extraction, within the hydrometallurgical step integrated into the beneficiation of the rare earth from the raw ore or from industrial process residues,[22,23] would be very economically and environmentally beneficial. Indeed, the chemical similarity of the rare earth forces a large number of time-consuming extraction steps to be taken, which require a large amount of non-recyclable chemicals.[23] This could be reduced if the differences in the magnetic moments of the rare earth ions could be exploited efficiently.

However, the application of such a magnetic separation step is still hampered by the insufficient understanding of the above-mentioned observations. Although the observations

are robust, the underlying mechanism is physically unclear. This was already addressed in our previous work, Ref.,[13] with reference to the huge difference in the order of magnitude between the kinetic energy of $3/2\ kT$ at a temperature T, associated with Brownian motion (k - Boltzmann constant), and the magnetic energy, proportional to the magnetic moment of the molecule times B. Hence, it actually seems unlikely that $\vec{f}_m$ has a direct influence on the paramagnetic ions.

To resolve this paradox, the concept of the effective magnetic susceptibility of nano- and micro-scale clusters of paramagnetic ions, called *magnions* was introduced in Refs.[18,24] Magnions represent a charged region of continuous medium in a liquid containing a large number of paramagnetic ions. If the theory of magnions can be substantiated, their much larger effective magnetic susceptibility compared to that of the single ions could indeed help to explain the above-mentioned findings.

The working hypothesis of this study is different and postulates that a hidden trigger process is involved in Refs.[13,15,16,20] Solvent evaporation is the most likely candidate. To verify the hypothesis of an evaporation-assisted magnetic separation, an experimental setup (Section 2) was developed in which a weak evaporation rate can be adjusted. Section 3 explains the physical processes in the cell and quantifies the resulting heat and mass transfer fluxes. To discriminate between the temperature and concentration contributions in the refractive index field, measured by Mach-Zehnder interferometry, a new algorithm is presented in Section 4. Numerical simulations of concentration and temperature fields are conducted to better understand their dynamics and respective impact on the refractive index field, see Section 5.2. Both works provide a basis for deriving the evolution of the rare earth ions concentration field in the cell, as shown in Section 5.3. A discussion of the results, including the hydrodynamic stability of the system in Section 6 leads to the safe conclusion that synergy between evaporation and field gradient force is the mechanism underlying the separation results discussed above. Section 7 provides a summary of the work and addresses remaining issues.

2 Experimental setup

The experimental container shown in Fig. 1 consists of three cells: the central measurement cell ($10\times10\times10$ mm^3), made of quartz glass in optical quality(1.25 mm thickness) which is surrounded by two identical seed cells, made of PTFE. All three cells are placed inside a base frame, manufactured from plexiglass. The measurement cell is completely filled with rare earth solution under study at a concentration of c_0 until a flat free interface is established. A rare earth solution of the same type but of a different concentration c is injected into the two neighboring cells. Then, the plexiglass base is closed with a lid using non-magnetic screws and a soft plastic pad to seal it. By this means, a closed system with good optical quality is constructed, which is placed into a Mach-Zehnder interferometer, see Section 4. The volume ratio of the solutions in the optical and seed cells and the vapor phase is close to 1:1:1.
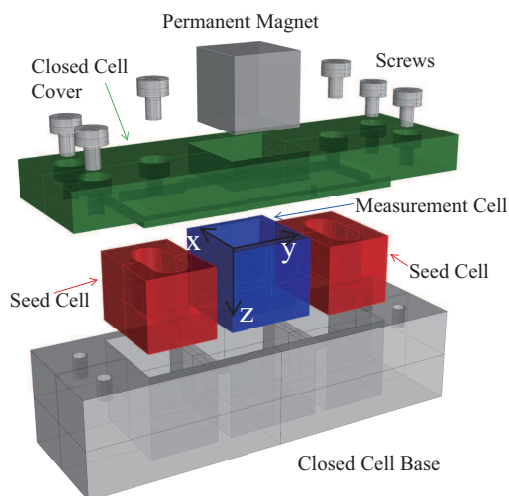

Figure 1: Schematic diagram of the setup consisting of an outer plexiglass cell(gray and green parts) which provides a closed system for mass, a high-quality optical quartz glass measurement cell, two seed cells made of Teflon and the NdFeB permanent magnet.

Three rare earth salt solutions with different concentrations (0, 0.5 and 1 M) are prepared using DyCl$_3$ hexahydrate (99.9 %, abcr GmbH & Co. KG) dissolved in deionized water. The pH is adjusted with hydrochloric acid. Given the equilibrium constant of Dy^{3+}, log $K_{s10} = $ 15.9 at 25°C,[25] a pH value of 5.3 results. Above this pH, precipitation and sedimentation

starts. Below this value, the solution is free of precipitated clusters, a fact which was verified by dynamic light scattering at pH=5. To completely rule out the formation of $Dy(OH)_3$ precipitates, pH=1 was chosen in the experiments and a Millex-LCR millipore 0.45 μm filter was used before filling the cell with the solution.

We consider the molar susceptibility of the solution in the cell as the sum of the susceptibility of the aqueous solution, $\chi_{sol,0}$, at Dy(III) concentration c_0 and pH=1 and a variation, resulting from a change in concentration $\Delta c = c - c_0$ due to solvent evaporation, multiplied by the molar susceptibility of dysprosium ($\chi_{Dy} = 5.5 \times 10^{-7} \mathrm{m^3/mol}$):

$$\chi_{sol} = \chi_{sol,0} + \chi_{Dy}\,\Delta c. \tag{2}$$

A permanent magnet of size $10 \times 10 \times 10$ mm^3 (Webcraft GmbH, remanence $B_r =$1280 mT, magnetization of N42) is used to provides a static inhomogeneous magnetic field. The magnet is placed on top of the closed cell at the center of a machined groove inside the lid. Its magnetization direction is oriented along the z direction. The vertical distance between the magnet and the free interface amounts to 3 mm.

The experiments were run at room temperature $(20 \pm 1)°$C and atmospheric pressure. The majority of the experiments lasts approx. 140 min, added by a few number of long-time experiments for up to seven days. The resulting volume loss due to evaporation was measured by analyzing shadowgraphs of the surface profile of the solution remaining in the measurement cells and is discussed later on.

The magnetic field is simulated using Ampere's law based on the same procedure as in reference[26] and shown in Fig. 2a for a quarter of the cells both as a 3D vector plot and as a contour plot. The resulting 3D magnetic field gradient force within the optical cell, calculated with Eq. (1), is plotted in the same manner in Fig. 2b. The dominant force component is that along z direction. In the cell, it reaches its highest value at the liquid-air interface and decreases rapidly along z. The force components in the x-y plane are not negligible, in
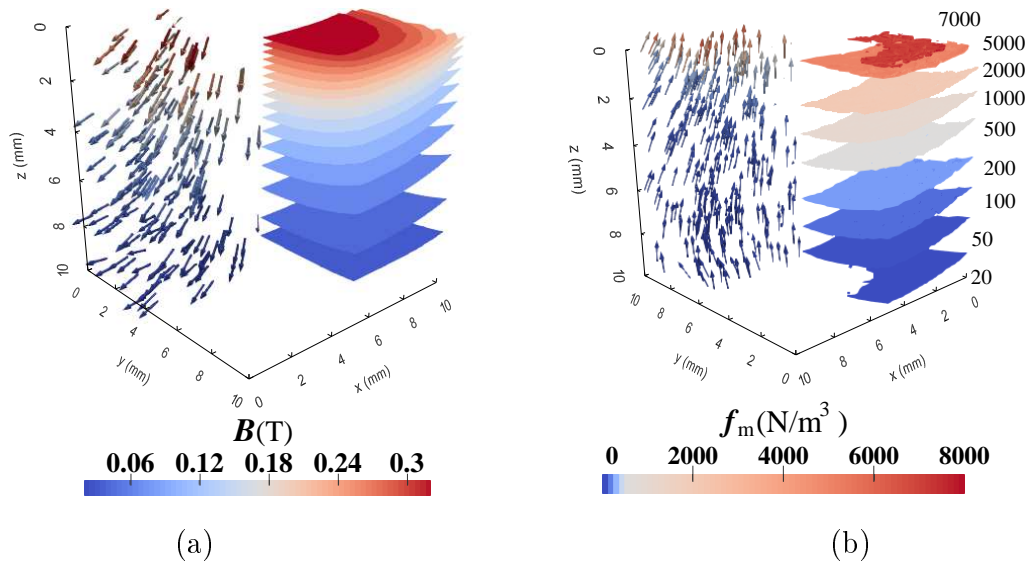
6

Figure 2: Simulated 3D (a) magnetic field and (b) field gradient force within the whole inner region of the plexiglass cell and measurement cell, respectively ($c_0 = 0.5$ M). Iso contour lines and vector field are scaled with same colorbar provided below for both sub-figure.

particular at the interface. They are oriented from the margin of the cell towards the center of the cell.

3   Physical picture

For the moment let us leave the magnetic field aside and consider the physical processes which take place at the liquid-gas interface of the dysprosium solution, see Fig. 3. While DyCl$_3$ salt is non-volatile, the water molecules evaporate in each of the three cells of Fig. 1 until the saturation partial pressure of the respective water solution, corresponding to the ambient temperature, is established. Consider the solution as an ideal one; its saturation pressures obey Raoult's law:

$$p_w = p_v(T)x_w, \tag{3}$$

i.e., the partial pressure of the water vapor above the solution depends not only on the saturation vapor pressure $p_v(T)$ of pure water but also on the mole fraction of water, x_w. Since the dysprosium concentration of the seed cell is twice as high as that of the measurement
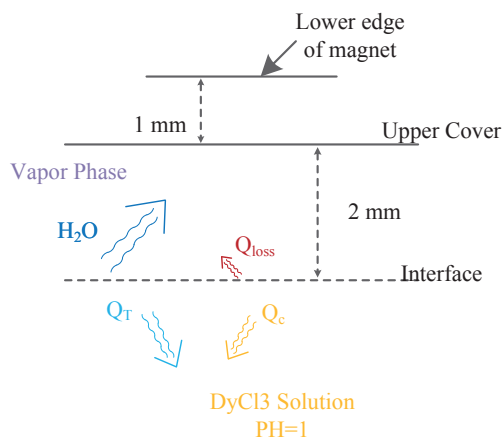
Figure 3: Illustration of physics corresponding to evaporation of water molecules and a zoom into the interface

cell, the mole fraction $x_w = n_w/(n_w + 2c_0V)$ in the seed cell is slightly lower than that in the measurement cell ($x_w = n_w/(n_w + c_0V)$), where n_w stands for the moles of water. As a result, the equilibrium vapor pressure is a bit lower there compared to the measurement cell. By means of this technique, the evaporation rate can be adjusted via the concentration difference between the seed and measurement cells. The resulting vapor pressure gradient in the gas phase forces further evaporation of water molecules from the solution with a lower concentration due to gas molecules in the vapor phase diffusing toward the cell with higher salt concentration. There, water molecules condense at the interface. Thus, the more concentrated solution experiences a slight dilution, while a concentration increase occurs in the less concentrated solution. In the course of this process, the driving pressure gradient in the vapor atmosphere of the cell is gradually diminished over a long period of time.

Evaporation is coupled with fluxes across the interface, where we now focus entirely on the measurement cell. First, there is a flux of solvent molecules into the gas phase. Hence, the mass of the solutions is not conserved only in its solute content. As a result, the volume of the solution decreases slightly. Correspondingly, a local concentration increase occurs near the interface. Thus, a source term for the concentration field appears. Second, a flux in terms of thermal energy occurs, since the latent heat for evaporation has to be provided. As a result, the local temperature below the interface decreases. This heat flux $Q(t)$ from

the boundary into the system is given by

$$\frac{\partial Q(t)}{\partial t} = -\Delta H_{vap} \cdot c_{water} \frac{\partial \delta V(t)}{\partial t} \qquad (4)$$

where $\Delta H_{vap} = 44kJ/mol$ and $c_{water} = 55.56$ mol/ L refer to the molar latent heat and molar concentration of water, respectively. Eq. (4) shows that the heat flux is a function of the evaporation rate, i.e. the volume loss $\delta V(t)$ of water per time unit. To obtain $\partial_t \delta V(t)$ we invoke the fact that the moles of solute ($DyCl_3$) dissolved in water, $n_0 = c_0 V_0$, is a conserved quantity during evaporation, where c_0 and V_0 refer to the initial concentration and volume of the solution. Hence

$$n_0 = c_0 V_0 = const = \bar{c}(t)(V_0 - \delta V(t)), \qquad (5)$$

i.e., a volume reduction forces the volume-averaged concentration of Dy(III), $\bar{c}(t)$, given by $\bar{c}(t) = \frac{1}{V} \iiint_V c(x,y,z,t)dxdydz$, to increase. Extracting δV from Eq.(5) and putting its partial derivative with respect to time into Eq.(4) we obtain

$$\frac{\partial Q(t)}{\partial t} = -\Delta H_{vap} \cdot c_{water} \cdot V_0 \cdot c_0 \cdot \bar{c}(t)^{-2} \cdot \frac{\partial \bar{c}(t)}{\partial t} \qquad (6)$$

This equation indicates that the heat flux across the surface during evaporation is a function of the initial concentration, initial volume and mean concentration change, and depends nonlinearly on the mean concentration. $\partial \bar{c}(t)/\partial t$ is assumed to be constant over the interface of the solution. This is justified by the fact that the weak evaporation, acting over times less than 140 min, leads to only marginal changes of the initially perfectly flat interface in the cell.

Once the source terms for the concentrations and temperature field have been specified, their transport inside the solution is governed by

$$\frac{\partial T}{\partial t} = \kappa \cdot \left(\frac{\partial^2 T}{\partial x^2} + \frac{\partial^2 T}{\partial y^2}\right) \qquad (7)$$

and

$$\frac{\partial c}{\partial t} = D \cdot \frac{\partial^2 c}{\partial x^2} \tag{8}$$

respectively, with a mass diffusivity of $D = 1 \times 10^{-9}$ m^2/ s and a thermal diffusivity of water given by $\kappa = 1.38 \times 10^{-7}$ m^2/ s. Since volume loss can be neglected for experiments shorter than 140 min, see Section 5.2), it is justified to approximate heat and mass transport as 2D and 1D processes, respectively. The transport proceeds by diffusion since the field-gradient force effectively suppresses any evaporation-driven convection, as we will show later on.

Eqs.(7-8) are solved by using a finite-difference method. The boundary condition for heat transfer is a Neumann boundary condition at the free interface of the solution and a mixed boundary condition for the heat losses at all other boundaries, i.e. $\frac{\partial q(t)}{\partial t}|_{z=0mm} = \frac{\partial Q(t)}{\partial t}/A_{interface} + S_{loss}$ where S_{loss} refers to the heat losses via the quartz walls of the cell. Since the dominant heat transfer takes place at the interface, it is legitimate to neglect S_{loss}. Harmonic conductivity, i.e. $k = \frac{k_{quartz} k_{fluid}}{k_{quartz} + k_{fluid}}$ is used at the boundary between the quartz and the solution. The initial conditions for the temperature and concentration are $T_0 = 20.0°$C and $c_0 = 0.5$ M, respectively, depending on the experimental conditions. The boundary flux value for mass and heat at the free interface is discussed in Section 5.1.

The target quantity which we use to describe the dynamics in a rare earth solution is the change in the refractive index, $\Delta n(\vec{r}, t)$, with respect to the reference field $n_0(c_0, T_0)$. This change, $\Delta n(\vec{r}, t)$, can be written as

$$\Delta n(\vec{r}, t) = \Delta n[T(\vec{r}, t), c(\vec{r}, t)] = \Delta n_T(\vec{r}, t) + \Delta n_c(\vec{r}, t) \tag{9}$$

where Δn_T and Δn_c refer to changes in Δn due to changes in temperature and concentration. The refractive index as a function of temperature changes as $\frac{\partial n}{\partial T} = -\frac{1}{10200}$ K^{-1}, see[27] while $\frac{\partial n}{\partial c} = \frac{1}{23.31002}$ (M)$^{-1}$ holds for that with the concentration of DyCl$_3$.[16] Thus it is obvious that a change in concentration has a greater weight than a change in temperature. This fact, together with the different transport dynamics of $\Delta T(\vec{r}, t)$ and $\Delta c(\vec{r}, t)$) due to their

different diffusivities, forms the basis for discriminating between $\Delta n_c(\vec{r}, t)$ and $\Delta n_T(\vec{r}, t)$, as will be explained next.

4   Interferometry and data processing algorithm

To determine $\Delta n(\vec{r}, t)$, Eq.9, a Mach-Zehnder interferometer (MZI) is used. The phase difference $\Delta\varphi(\mathbf{x})$ between the cell under study and an isothermal reference cell, as measured by the MZI, relates to the difference in the refractive index Δn as follows:

$$\Delta n = \frac{\Delta\varphi(\mathbf{x}) \cdot \lambda}{2\pi l} \tag{10}$$

where $\lambda = 632.8$ nm is the wavelength of the He-Ne laser. l stands for the characteristic length of the beam passing through the optical cell. To obtain $\Delta n(x, y, t)$, the phase difference $\Delta\varphi(\mathbf{x}, \mathbf{t})$ has to be extracted from the interferograms, cf. our previous works.[26,27] Its time and space domain resolution is determined by the sampling frequency and the number of pixels of the CCD, respectively. The actually measured refractive index, $\Delta n_m(\vec{r}, t)$, using Eq. (9), is affected by noise, $n_n(t)$, as detailed in:[26]

$$\Delta n_m(\vec{r}, t) = \Delta n_c(\vec{r}, t) + \Delta n_T(\vec{r}, t) + n_n(t) \tag{11}$$

To get rid of $n_n(t)$ and gain access to the contributions $\Delta n_c(\vec{r}, t)$ and $\Delta n_T(\vec{r}, t)$, here we introduce an algorithm for data post-processing which we call a two-step compensation algorithm. This algorithm takes into account the dynamics of mass and heat transport in the system. Referring to the physical picture, given in Fig. 3, the mass and heat in the system can be considered as the sum of a conserved field and corresponding flux terms across the boundaries. We combine the conserved parts and time-dependent transient parts of heat and mass into a conserved field $\Delta n_{cons}(\vec{r}, t)$ and a time-dependent transient term $\Delta n_t(t)$,

respectively. This allow to rewrite Eq. (11) into

$$\Delta n_m(\vec{r},t) = \Delta n_{cons}(\vec{r},t) + \Delta n_t(t) + n_n(t), \tag{12}$$

The definition of the conserved part of the refractive index field is that its integration over the field of view $A = Y \cdot Z$ (Y=Z=10 mm) gives

$$\iint \Delta n_{cons} dA = 0. \tag{13}$$

Thus its derivative with respect to time also vanishes:

$$\partial_t \iint \Delta n_{cons} dA = 0. \tag{14}$$

Note that a matrix is hidden beyond each refractive index field, given by the resolution of the camera (1600 x 1200). Making use of Eq.(13) and integrating Eq.(12) along the y-z plane in space, we obtain

$$\begin{aligned}
\iint \Delta n_m dA &= \iint \Delta n_{cons} dA + \iint \Delta n_t dA + \iint n_n dA \\
&= 0 + \Delta n_t \cdot A + n_n(t) \cdot A
\end{aligned} \tag{15}$$

Eq.(15) offers us two possibilities. In the first step, the time-dependent transient part Δn_t can be obtained via:

$$\Delta n_t = \frac{1}{A} \iint \Delta n_m dA - n_n(t), \tag{16}$$

The noise term $n_n(t)$ is not known beforehand. However, the analysis of the results shown later in Fig. 4 demonstrates that the noise in the experiment is both of a significantly higher frequency and of a much smaller amplitude than Δn_t. Therefore, a suitable fitting of Δn_t as carried out in Section 5.1 eliminates $n_n(t)$ and allows to extract Δn_t in the first step of the algorithm.

Differentiating Eq.(15) with respect to time under the constraint of Eq. 14 delivers

$$
\begin{aligned}
\partial_t \iint \Delta n_m dA &= (\partial_t \Delta n_t + \partial_t n_n) \cdot A \\
&= \partial_t (\Delta n_t + n_n) A.
\end{aligned}
\tag{17}
$$

Upon invoking Eq.(12), Eq.(17) leads to

$$
\partial_t \iint \Delta n_m dA = \partial_t (\Delta n_m - \Delta n_{cons}) A.
\tag{18}
$$

Integrating Eq.(18) we obtain, in the second step of the algorithm, the desired Δn_{cons} by

$$
\Delta n_{cons} = \Delta n_m - \frac{\iint \Delta n_m dA}{A}.
\tag{19}
$$

5   Results

We next apply this algorithm to analyze the dynamics of the refractive index field Δn_m, Eq.(12), in the $DyCl_3$ solution, where the following strategy is pursued: We first determine the transfer part Δn_t by fitting the experimental data. Using $\partial_t \Delta c = \frac{1}{\partial n/\partial c} \partial_t \Delta n_t$ we are able to specify the boundary mass flux $\frac{\partial \bar{c}(t)}{\partial t}$ needed to obtain the boundary heat flux, Eq. (6). This allows the temperature and concentration field to be simulated by means of which we can study the respective contributions, Δn_T and Δn_c, in the two-stage evolution found for Δn_t. Finally, we use this information to convert the computed Δn_{cons}, calculated in the second step of the algorithm via Eq.(19), into the concentration field of the $Dy(III)$ ions.

5.1   Dynamics of the refractive index field component Δn_t

We study the evolution of Δn_t for both evaporation and condensation in the measurement cell. We start with evaporation, as presented in Fig. 4a. This figure contains the raw data of one measurement (red triangles) together with the error band obtained from the standard

deviation of three independent measurements. Each measurement i can be fitted using the logarithmic function $\Delta n_t = a_i + b_i ln(t + c_i)$. On averaging the fits of three independent experiments (solid curve in Fig. 4a) we obtain $\bar{a} = -2.8608 \times 10^{-4}$, $\bar{b} = 0.55765 \times 10^{-4}$ and $\bar{c} = 169$. Characteristic changes in Δn_t occur in the order of 10^{-4}.

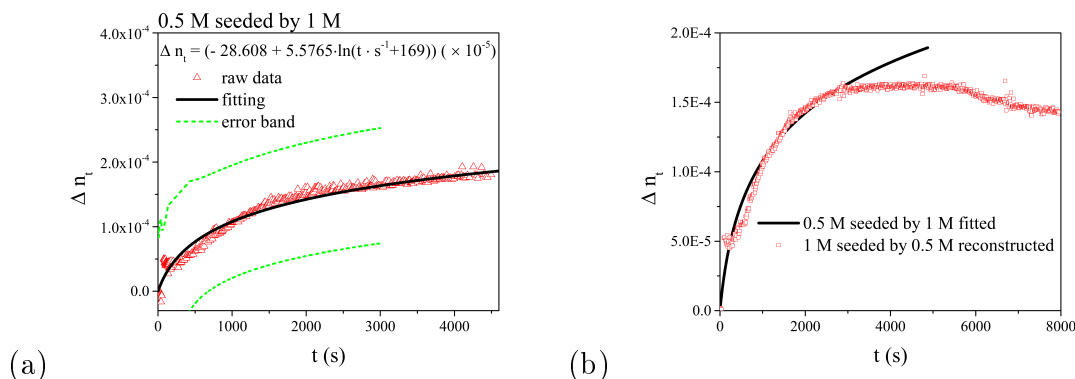(a)   (b)

Figure 4: Change of the refractive index component Δn_t, eq.(16), as a function of time: (a) evaporation case (0.5 M seeded by 1 M). The error band is a obtained via the standard deviation of fitting curve of 3 independent repeating experiments. (b) Condensation case (1 M seeded by 0.5 M) in comparison with the evaporation case (solid line).

The origin of this variation of Δn_t is the transfer of water molecules and the resulting concentration increase accompanied by a temperature decrease. Given the opposite signs of $\frac{\partial n}{\partial T}$ and $\frac{\partial n}{\partial c}$, an increasing Δn_t indicates that water is evaporating from the measurement cell, i.e. as represented by Fig. 4. We note a two-stage evolution with a larger $\partial_t \Delta n_t$ in the first phase and a smaller one in the second phase. Before interpreting this behavior, we compare it in Fig. 4b with that found in the case of condensation when water vapor condenses in the measurement cell. Remarkably, the evolution of $\partial_t \Delta n_t$ in the first phase is identical with that in the case of evaporation. A divergence in the evolution of Δn_t occurs beyond $t_{cross} \approx 2000$ s. From that moment on, Δn_t decreases in the case of condensation while further increasing in the case of evaporation. From the identical evolution in the first phase, we can conclude that the same process obviously take place first, irrespectively of whether the system is prone to condensation or evaporation due to the concentration differences imposed. This process is the evaporation of water molecules until the saturation vapor pressure is achieved as shown
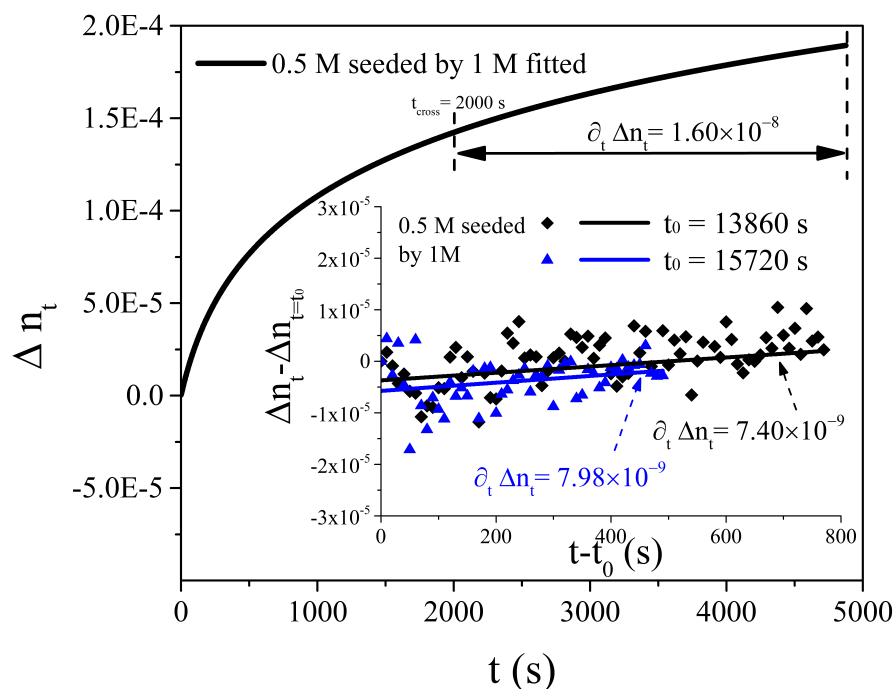
Figure 5: Δn_t as a function of time (0.5 M seeded by 1 M) ranging from 0 s to 4500 s. The inserted figure includes two independent long-term measurements of Δn_t in the case of continuous evaporation shown starting from $t_0 = 13860$ and 15720 s, respectively.

in Eq.(3). The subsequent second phase is then governed by the diffusion of water vapor molecules between the measurement and seed cells depending on the differences in the vapor pressure adjusted by the respective concentrations.

Thus, we can conclude that in the first phase, due to the higher evaporation, both temperature and concentration changes contribute to Δn_t, as also proved in Section 5.2. The second stage, characterized by a weaker slope of Δn_t, is dominated by the concentration contribution due to the decay in the temperature effect. The cross-over time between the two phases, $t_{cross} \approx 2000$ s, marks the moment at which $p_v \approx p_v^{sat}$. We found similar t_{cross} for 0.5 M and the 1 M solution, despite their differences in thermodynamic properties. Hence, the second phase enables us to estimate the rate of the concentration change,

$$\frac{\partial c(t)}{\partial t} = \frac{\partial c}{\partial n} \cdot \frac{\partial \Delta n_t}{\partial t}, \tag{20}$$

due to solvent evaporation since the temperature contribution is now negligible. The required $\partial_t \Delta n(t)$ is plotted for three different experiments in Fig. 5. First, it is given as a fit of the data in Fig. 4a from $t_{cross} \leq t \leq 5000$ s leading to $\partial_t \Delta n_t = 1.60 \times 10^{-8}$, or $\partial_t c(t) \approx 3 \times 10^{-7}$ M/ s. Second, two long-term experiments were performed, see inset, which lead to nearly identical results. On fitting the data in the intervals $t_0 \leq t \leq t_0 + 800$ s with $t_0 = 13860$ s and $t_0 \leq t \leq t_0 + 450$ s with $t_0 = 15720$ we obtain $\partial_t \Delta n_t \approx 7 \times 10^{-9}$, or $\partial_t c(t) \approx 2 \times 10^{-7}$ M/s. We finally compare this with a 7-day experiment in which a volume loss of 5.4% was detected, which is equivalent to $\partial_t \Delta n_t \approx 3.9 \times 10^{-10}$ s^{-1}. As expected, on the way to thermodynamic equilibrium, hence vanishing vapor pressure differences between measurement and seed cells, we observe a slowly declining evaporation rate which simultaneously decreases $\partial_t \Delta n_t$ and correspondingly $\partial_t c(t)$. As a conservative estimation for the latter we take $\partial_t c(t) \leq 3 \times 10^{-7}$ $mol/(l \cdot s)$.

5.2 Supporting heat and mass transfer analysis

With the given $\frac{\partial c(t)}{\partial t}$, the heat flux, $\partial Q(t)/\partial t$ (Eq. 6) can be calculated and shown in Fig. 6a as a function of $\bar{c}(t)$ and $\frac{\partial \bar{c}(t)}{\partial t}$. It is obvious that $\partial Q(t)/\partial t$ is much more sensitive with respect to $\partial \bar{c}(t)/\partial t$ than to $\bar{c}(t)$. Since the time span which is relevant to the measurements consists in the initial 2 hours of magnetization, we can therefore safely set $\bar{c}(t) \approx 0.5$ M. This now allows for an explicit calculation of the heat flux $\partial Q(t)/\partial t$ as a function of $\partial \bar{c}(t)/\partial t$ as shown in Fig. 6b. For the concentration under study ($c_0 = 0.5$ M) we obtain $\frac{1}{A_0}\frac{\partial Q_{heat}}{\partial t} = -4.89 \times 10^3 \frac{J}{M} \frac{1}{A_0} \frac{\partial c(t)}{\partial t} = -14.67$ W/ m^2, which is the corresponding heat flux due to the evaporation of water molecules. We use this value as the boundary condition for the simulation of the temperature field inside the cell, Eq. (7) in Section 3, which is plotted in Fig. 7. We note three important facts:

1. As expected, the temperature field has a 2D behavior due to heat exchange between the fluid and the quartz glass.
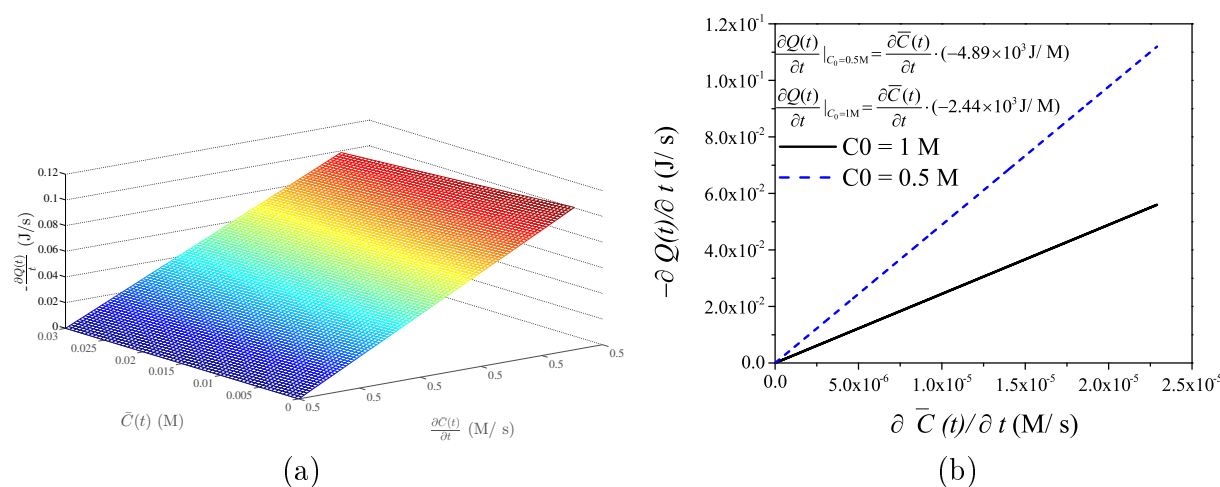
Figure 6: (a)Heat flux as a function of mean field concentration and the rate of concentration change ($c_0 = 0.5$ M) and (b) Heat flux as a function of the rate of concentration change.

2. The temperature of the solution decreases due to the evaporation. Given the rather high diffusivity of the solution, the temperature inhomogeneity is more significant along time than space and the average temperature decreases by about -0.35 K after 1000 sec.

3. At the same time we note that the temperature difference between the interface and the bottom of the cell does not exceed 0.1 K. The spatial gradient of temperature does not change dramatically after 500 s.

The temperature field gives rise to a corresponding refractive index field via $n(y, z) = T(y, z)\partial n/\partial T$. The latter can be translated into a fictitious concentration field using $c(y, z) = n(y, z)/\partial n/\partial c$. This fictitious concentration field, mimicked by temperature changes, is plotted in Fig. 7b.

As we can see from Fig. 7b, the temperature field is responsible for a spatial concentration difference of approximately 0.15 mM at a representative time t=500 s. On comparing this with the concentration change of 2 mM in Fig. 9, we clearly see that the temperature contribution, although present, amounts to less than 10% of the concentration change derived from the measured refractive index.
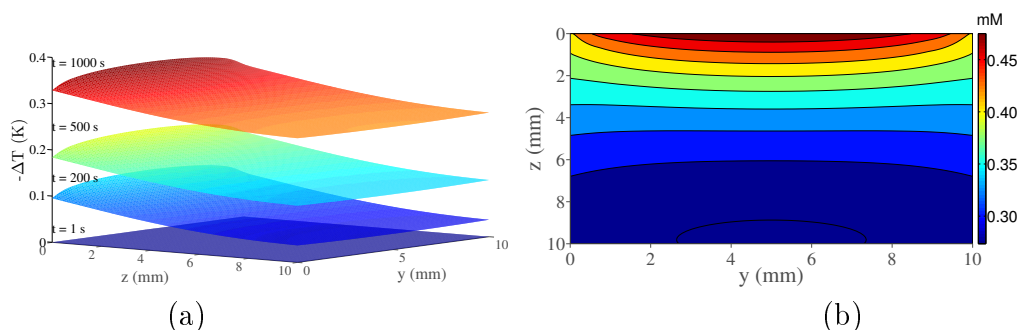
(a) (b)

Figure 7: (a)2D simulation result of temperature field at t= 1, 200, 500 and 2000 s after evaporation has started at the liquid-gas interface and (b) fictitious concentration field due to a change in the temperature field at t = 500 s.

To further support the validity of a discrimination between Δn_T and Δn_c, eq. (9) we next compare the dynamics of the temperature field with that of the concentration field. For this purpose, in Fig. 8 we show one-dimensional plots of T(z,t) and c(z,t) along the center of the x-y plane (x= 5 mm, y= 5mm). It can clearly be seen that the heat transfer
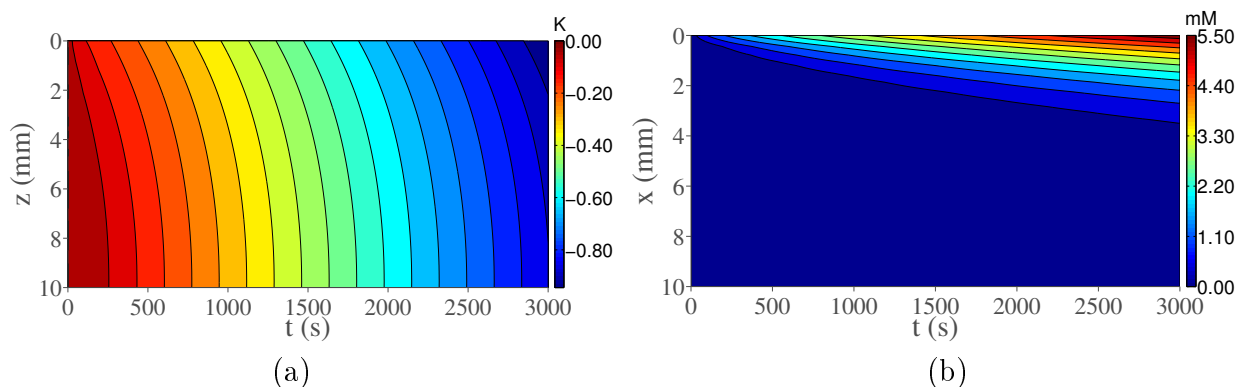

(a) (b)

Figure 8: 1D plots of temperature (a) and concentration (b) as function of t and z at the center of the plane (x=5 mm; y=5 mm) as obtained by simulation.

reaches a stationary state in which the gradient of temperature along the z direction is constant. By contrast, due to the low diffusivity of the solute compared to that of heat, the diffusion process of the concentration field (Fig. 8) is still in a developing stage after 3000 s. Both facts about the temperature field, namely that it (i) falsifies the concentration field, derived from $n(\vec{r})$, by not more than 10% and (ii) already approaches a steady state while the concentration field is still developing, justify the validity of the translation into concentration units in Fig. 9.

5.3 Dynamics of the refractive index field component Δn_{cons}

We next perform the second step of the algorithm and apply Eq. (19) to determine Δn_{cons}. The analyses in Sections 5.1 and 5.2 have provided the necessary information for this purpose: (i) The overall time-dependence in the initial phase is mainly caused by the temperature decrease due to evaporation. (ii) The concentration and temperature field decouple on a longer time scale due to their different diffusivities and (iii) the temperature contribution is marginal after t_{cross}. These considerations clearly justify the conversion of conserved part, Δn_{cons}, into the concentration field, which is done via a division by $\frac{\partial n}{\partial c} = \frac{1}{23.31002}$ $(M)^{-1}$ and shown in Fig. 9. The most important issue visible in Fig. 9 is the formation of an oval region of elevated Dy(III) enrichment below the interface. This region continues to expand slowly between 60 s and 2000 s. The concentration iso-contour line resembles that of the magnetic field gradient force, cf. Fig. 2b. This process is entirely governed by diffusion. There is no convective contribution detectable.

Another feature of Fig. 9 is the formation of boundary layers at the vertical and horizontal quartz glass walls of the cell. Actually, these are fictitious concentration boundary layers caused by a small heat transfer across the quartz walls which was not taken into account in the simulations. As expected, this transfer is weaker at the sidewalls, due to the isolating effect of the surrounding air, and stronger at the bottom because of the higher heat conductivity of plexiglass (0.2 W/m^{-1}·K^{-1}). They slowly expand until the temperature field reaches a steady state.

It is useful at this stage to recall again the essence of the two-step compensation algorithm. In the first step, $\Delta n_t(t)$ was determined. Analyzing this enabled the temperature and concentration field to be decoupled over time and showed that in the second phase the temperature contribution vanished. In the second step, Δn_{cons} was obtained, showing the decoupling of the temperature and concentration field in space. As a result, it was possible to unambiguously correlate the computed concentration field at the oval part shown at the top of each subfigure of Fig. 9 with the enrichment of Dy(III) ions in this region. However,
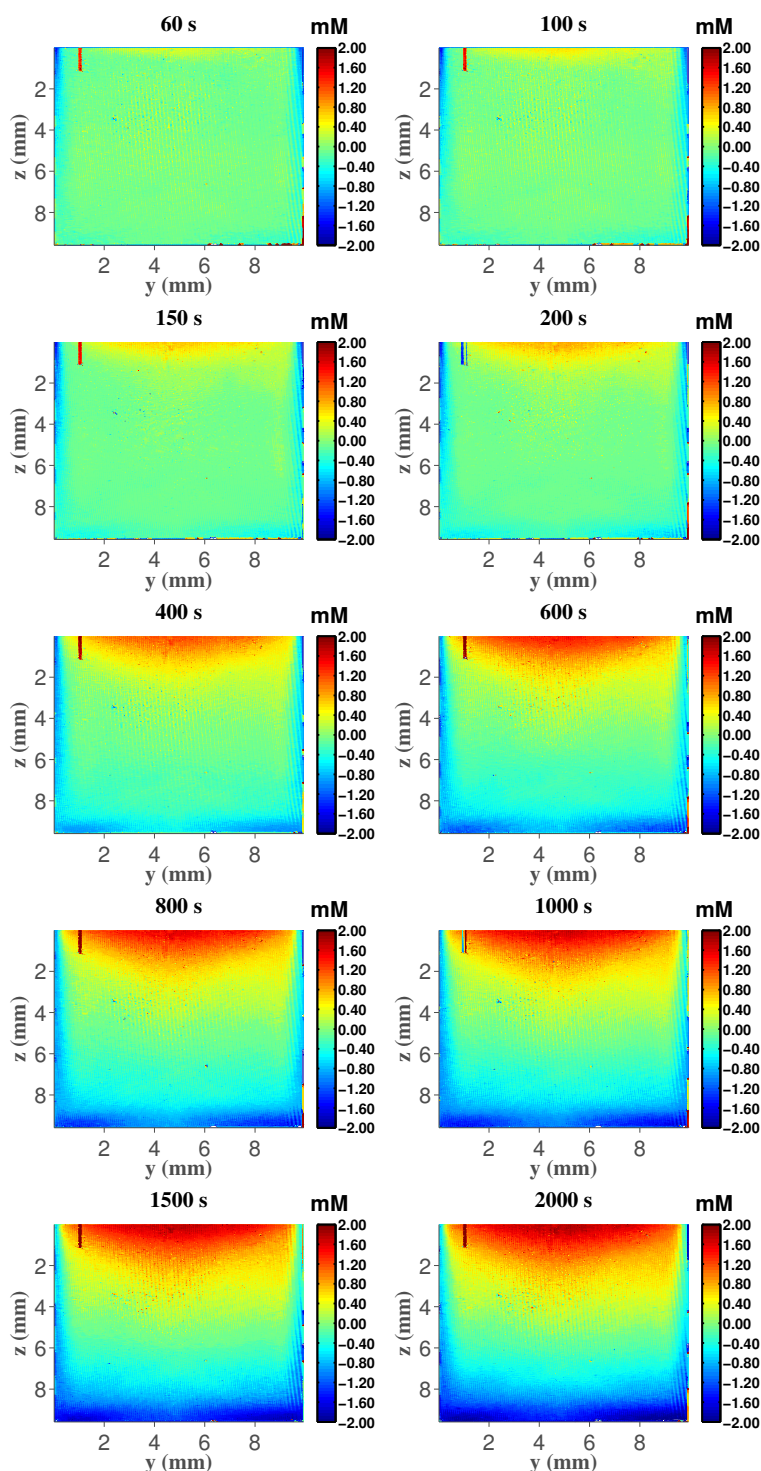
Figure 9: 2D concentration field in 0.5 M DyCl$_3$ solution, seeded by 1 M DyCl$_3$ solution, measured with interferometer between 60 s and 2000 s after the magnetic field is applied and evaporation starts. Along the lateral and bottom boundaries the contribution of a fictitious concentration field generated by the temperature field is visible.

the total concentration enrichment is given by the sum of Δn_{cons} (Fig. 9) and Δn_t (Fig. 4a), divided by $\frac{\partial n}{\partial c}$. Taking into account the temperature contribution to Δn_t in the first phase, a conservative estimation of the maximum enrichment amounts to 2 mM, cf. Fig. 9.

6 Discussion

The experimental results in Fig. 9 show the transport of both Dy(III) ions and heat in the presence of the magnetic field gradient force under the condition of a continuous weak evaporation. With the two-step compensation algorithm which was developed, we were able to "decouple" the concentration field from the temperature field in the sense of their spatial distribution and its variation in time. In conjunction with simulations of the development of both fields under experimentally specified boundary conditions (Section 5.2) we showed that more than 90% of the measured change in the refractive index of the weakly evaporating DyCl$_3$ solution is caused by the local increase in the Dy(III) concentration in the field gradient (Fig. 9).

The experimental setup in the present work was designed similarly to that of our former works.[13,16] The marked difference is that a free interface is admitted here at which weak evaporation is forced in terms of a vapor diffusion in a closed system. The similarity of the results obtained strongly suggest that evaporation is the missing puzzle piece necessary to understand the physics behind the robust enrichment of RE ions in the field gradient.

Evaporation proceeds in two phases inside the experimental cell. First, depending on the concentration, the respective saturation pressure in each cell is approached in the comparatively rapid first phase. Second, the vapor pressure differences due to the different concentrations sustain a diffusional vapor flux between the cells, giving rise to a lower evaporation rate in the second phase. These assertions were proved by a condensation experiment in Section 5.1. Generally, the evaporation of water molecules leads to the formation of a boundary layer of higher Dy(III) concentration at the surface. This concentration increase,

$\Delta c = c - c_0$, has two consequences. First, it increases the magnetic susceptibility in this zone by $\Delta\chi_{sol} = \chi_{Dy}\Delta c$ due to Eq.(2). Second, the density is elevated by $\Delta\rho = \rho - \rho_0 = \rho_0\alpha\Delta c$, resulting from a positive densification coefficient $\alpha = 0.243$ M^{-1}.[16] As a result, a heavier enrichment layer overlies a less dense bulk solution. Without a magnetic field, this boundary layer is hydrodynamically unstable, as discussed below. However, in the presence of the field gradient force no instability is observed. To understand this we start with the hydrostatic equation

$$\nabla p = \vec{f_g} + \vec{f_m} = g(\rho_f + \frac{\chi_{sol}}{2\mu_0 g}\frac{\partial\vec{B}^2}{\partial z})\vec{e_z} + \frac{\chi_{sol}}{2\mu_0}\nabla\vec{B}^2\mid_{xy} \tag{21}$$

where $\vec{f_g}$ and $\vec{f_m}$ represent the densities of the gravitational and magnetic field gradient force and $\nabla\vec{B}^2\mid_{xy} = \frac{\partial\vec{B}^2}{\partial x}\cdot\vec{e_x} + \frac{\partial\vec{B}^2}{\partial y}\cdot\vec{e_y}$. Eq. (21) contains two vertical force components: gravity, pointing downwards, and the z-component of $\vec{f_m}$, pointing upwards, as well as the radial component of $\vec{f_m}$, acting in the horizontal plane. Note that the first term on the right-hand side suggests that an apparent density $\rho_{app} = \rho_f + \frac{\chi_{sol}}{2\mu_0 g}\frac{\partial\vec{B}^2}{\partial z}$ could be introduced. This expresses the fact that the fluid density ρ_f is slightly tuned by the magnetic field gradient, which forms the basis of ferrohydrostatic separation.[2] We next invoke the dependence of ρ_f and χ_{sol} on the concentration change Δc to write

$$\nabla p = g(\rho_0 + \frac{\chi_{sol,0}}{2\mu_0 g}\frac{\partial\vec{B}^2}{\partial z})\vec{e_z} + \frac{\chi_{sol,0}}{2\mu_0}\nabla\vec{B}^2\mid_{xy} + (\rho_0\alpha g\Delta c + \frac{\chi_{Dy}\Delta c}{2\mu_0}\frac{\partial\vec{B}^2}{\partial z})\vec{e_z} + \frac{\chi_{Dy}\Delta c}{2\mu_0}\nabla\vec{B}^2\mid_{xy} \tag{22}$$

where $\chi_{sol,0}$ refers to the susceptibility at c_0. In the absence of evaporation, i.e. $\Delta c = 0$, only the first two terms of Eq. (22) are different from zero. In a closed cell, the system is completely stable, since there are no unbalanced force components because the concentration and susceptibility are spatially uniform. The action of $\vec{f_g}$ and $\vec{f_m}$ is now compensated for by the normal reaction from the walls. This is in agreement with other works[24,28] according to which fluids can only be manipulated based on the magnetic field gradient in the case of non-homogeneous liquid media, i.e. differences in susceptibility. Strictly speaking, the

presence of the free surface at $\Delta c = 0$ additionally requires the Moses effect to be taken into account.[11] It describes the elevation of the free surface of an otherwise homogeneous fluid, i.e. $\Delta c = 0$, to become an isoline of the magnetic pressure. However, this effect is very small here and can be neglected.

If $\Delta c \neq 0$, the situation becomes more involved. Eq. (22) shows that in the horizontal plane there is an unbalanced component of $\vec{f}_m$, as $\vec{f}_g$ acts only in the vertical direction. Fig. 10a plots this radial component of f_m inside the solution at different heights below the interface. Note that the vertical distance between magnet and interface is 3 mm. $\vec{f}_m(r)$ is the largest at the rim of the cell and vanishes at the center of the cell. With increasing distance from the magnet, the magnitude of the force components is drastically reduced. Generally, $\vec{f}_m(r)$ points inwards towards the center of the cell.
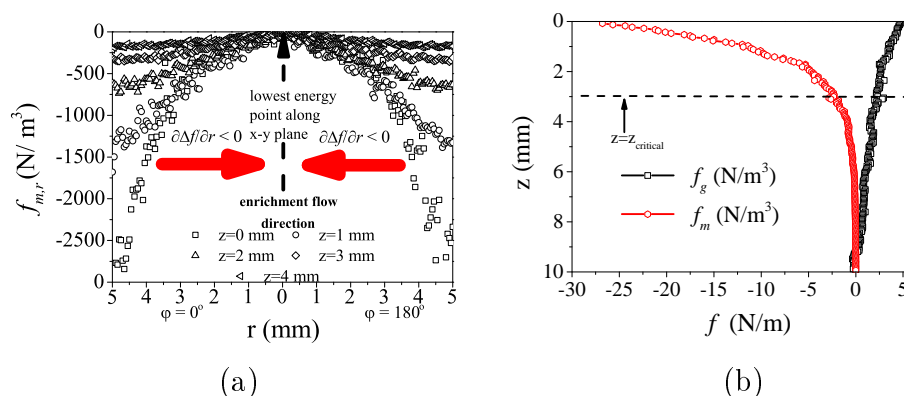

Figure 10: (a) Radial component of the magnetic field gradient force at different heights below the interface ($c_0 = 0.5$ M). A cylindrical coordinate system is used with the polar plane center at x=y=5 mm. A positive azimuthal direction for ϕ is therefore anti-clockwise. (b) Vertical force components Δf_m and Δf_g, referring to the terms in Eq. (21) containing a Δc. Δf_g is computed at t = 600 s with a concentration processed by two-step compensation along z at y = 5 mm, averaged along x.

Hence, fluid elements in the boundary layer are pushed horizontally from the rim of the cell towards the center. This is the mechanism by which the originally planar Dy(III) ion boundary layer, established by evaporation at the interface, is transformed into the concave region visible in Fig. 9.

Actually, in the presence of a concentration gradient, and hence a susceptibility gradient,

the rotation of the field gradient force, $\nabla \times \vec{f}_m$, no longer vanishes.[11,29] Thus there must be a microconvection beyond the resolution of our measurements, driving the transformation in the boundary layer from its initially planar shape towards a concave shape. However, in the absence of a macroscopically detectable velocity, we assume that hydrostatic Eq.(21) is approximately valid for a semi-quantitative explanation of the magnetic separation process.

To answer the question of why the concave enrichment boundary layer is levitated by the vertical force components in Eq.(22) instead of falling, we inspect the corresponding Rayleigh number of the boundary layer. The Rayleigh number quantifies the force of the layer by gravity in relation to the dissipative effects, mass diffusivity and viscosity. It is given by $Ra = -\frac{g\alpha \frac{\partial c}{\partial z} l_c^4}{D\nu} = -\frac{l_c^4}{D\mu} \frac{\partial \vec{f}_g \cdot \vec{e_z}}{\partial z}$, where the minus was introduced because $\partial f_g / \partial z < 0$ and $\vec{f}_g \cdot \vec{e}_z > 0$. Taking the values in Fig. 9, we obtain $Ra \approx 3 \times 10^4$. This value considerably exceeds the critical Rayleigh number $\mathrm{Ra}_{critical} = O(10^3)$.[30] Thus, this configuration is prone to a Rayleigh-Taylor (RT) instability, frequently also termed "density fingering" when it occurs in miscible liquids. However, no RT instability is observed in the presence of $\vec{f}_m$, as already stated above.

The reason for this is that the stability is modified by $\vec{f}_m$. The impact of $\vec{f}_m$ could be theoretically quantified by introducing a magnetic Rayleigh number similar to the case thermomagnetic convection.[31-34] Let us consider a layer of ferrofluid exposed to both a vertical magnetic field gradient and to a stabilizing temperature gradient due to heating from above.

Since the magnetization is a function of temperature, a fluid element undergoing a small adiabatic upward motion exhibits a higher magnetization than its surroundings. As a result, it experiences a magnetic force in the direction of the field gradient. Hence the perturbation reinforced and the originally quiescent ferrofluid layer is destabilized by the onset of convection, provided the critical magnetic Rayleigh number is exceeded. Despite some similarities, our present problem differs from thermomagnetic convection with regard to several issues, such as much lower susceptibility and a susceptibility gradient generated dynamically

by a concentration gradient instead of a temperature gradient. Furthermore, no theory has

been developed for our case, and hence there are no defined critical Rayleigh numbers.

For that reason we qualitatively explain how the gravitational force, acting downwards

parallel to $\vec{e_z}$ $(\vec{f_g} \cdot \vec{e_z} > 0)$, is reduced by the field gradient force $(\vec{f_m} \cdot \vec{e_z} < 0)$ acting in the

opposite direction. We seek to mimic the stabilization provoked by the field gradient using

a modified Rayleigh number Ra^*

$$\text{Ra}^* = -\frac{l_c^4}{D\mu}\frac{\partial \vec{f} \cdot \vec{e_z}}{\partial z} = -\frac{l_c^4}{D\mu}\frac{\partial (\vec{f_g} + \vec{f_m}) \cdot \vec{e_z}}{\partial z} \tag{23}$$

Forcing enters the Rayleigh number via the derivative with respect to z. Upon comparing

the respective derivatives of $\vec{f_g}$ and $\vec{f_m}$ in Fig. 10b it becomes obvious that $\partial f_g / \partial z$ is approx-

imately five times smaller than $\partial f_m / \partial z$. That is, the latter overcompensates for the gravita-

tional force and modifies the Rayleigh number of the layer, hence Ra^* becomes subcritical,

i.e. $\text{Ra}^* << Ra_{crit}$. This is the physical mechanism of the levitation of the Dy(III)-ion enri-

chment layer observed. It finally manifests in the fact that the iso-concentration lines follow

the contour lines of the magnetic pressure, as becomes obvious when Fig. 11a is compared
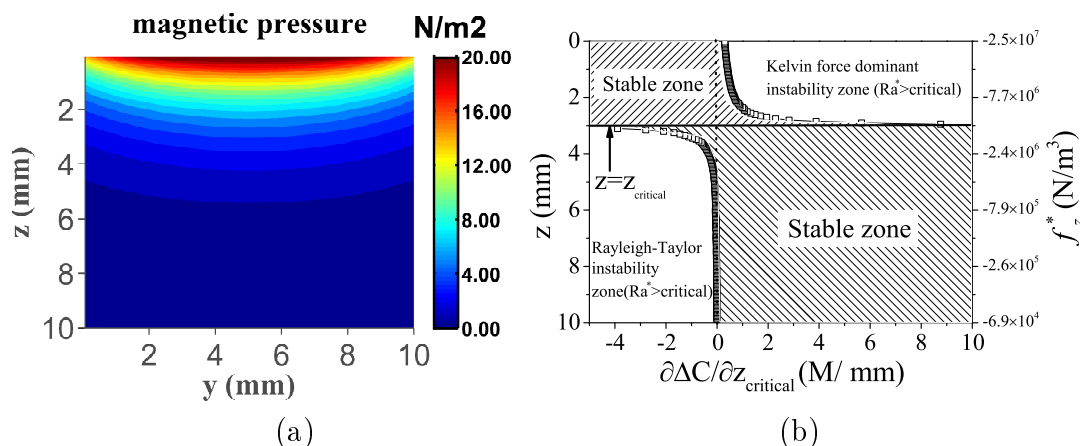
with Fig. 9.

Figure 11: (a) Magnetic pressure isolines and (b) stability diagram, $\frac{\partial \Delta c}{\partial z}\big|_{Ra^\star=0}$ vs. z-coordinate at $c_0 = 0.5$ M.

Having clarified the mechanism of paramagnetic levitation, we next attempt to specify

the critical concentration gradient of the paramagnetic ions which can be kept stable by the magnetic field gradient. We make a very conservative estimation by taking $Ra^* = 0$ as the respective condition. That is, we determine the gradient $\frac{\partial \Delta c}{\partial z}\mid_{Ra^*=0}$ at which the field gradient force nullifies the force by gravity:

$$Ra^* = 0 = \frac{\partial(\vec{f_g} + \vec{f_m}) \cdot \vec{e_z}}{\partial z} = \frac{\partial(\rho_0 g(1 + \alpha\Delta c) + \frac{(\chi_{sol,0} + \chi_{Dy}\Delta c)}{2\mu_0}\frac{\partial \vec{B^2}}{\partial z})}{\partial z} \tag{24}$$

With $\vec{f_{z0}} = f_{z0} \cdot \vec{e_z} = \frac{1}{2\mu_0}\frac{\partial \vec{B^2}}{\partial z} \cdot \vec{e_z}$ we obtain

$$\frac{\partial \Delta c}{\partial z}\mid_{Ra^*=0} = -\chi_{sol,0} \cdot \frac{\frac{\partial f_{z0}}{\partial z}}{\rho g \alpha + \chi_{Dy}f_{z0}} \tag{25}$$

$\partial \Delta c/\partial z\mid_{Ra^*=0}$ depends on two variables: on the c_0 which enters $\chi_{sol,0}$, and on the distribution of the magnetic field, determining f_{z0} and its derivative. Since the influence of c_0 is very weak and can be neglected, the main impact results from f_{z0}. Due to its negative sign, Eq. (25) possesses a singularity at $f_{z0} = -\frac{\rho g \alpha}{\chi_{DyCl_3}} \approx -4.32 \times 10^6$ N/m^3. This value can be converted into the corresponding z coordinate. For the magnetic field used in our setup, we obtain $z_{crit} \approx 3$ mm. Actually, the lines $z = z_{crit}$ and $\partial \Delta c/\partial z\mid_{Ra^*=0} = 0$ divide the stability behavior of our system into 4 quadrants, see Fig. 11b. In two of them, the upper left quadrant and the lower right one, the system is stable. Our system, characterized by $\partial \Delta C/\partial z < 0$, falls into the upper left quadrant, which is bounded by $z < z_{crit}$ and $\partial \Delta c/\partial z\mid_{Ra^*} \leq 0$. Our concave boundary layer, enriched in Dy(III) ions, is unconditionally stable, irrespectively of the magnitude of the negative concentration gradient established. This is due to the dominance of the field gradient force over the gravitational force for $z < z_{crit}$ and the linear dependence of both the density and susceptibility on the concentration, which keeps the force ratio unchanged. A second stable quadrant is the lower right one, encompassed by $z > z_{crit}$ and $\partial \Delta c/\partial z\mid_{Ra^*=0} \geq 0$. Since the density decreases along with the concentration, this quadrant is characterized by a stable density stratification not perturbed by the weak field gradient.

By contrast, the system can become unstable in the non-shaded regions. Although these two types of instability are both directly related to the concentration distribution, they differ from each other intrinsically. The instability in the lower left quadrant is caused by the density gradient, while that in the upper right quadrant has its origin in the susceptibility gradient. We first look at the lower left quadrant, bounded by $z > z_{crit}$ and $\partial \Delta c / \partial z \mid_{Ra^*=0} \leq 0$. In this zone, the field gradient force is weak and of the same order as the gravitational one. Hence, for $Ra > Ra^\star = 0$, an existing unstable density stratification can give rise to the onset of Rayleigh Taylor instability, forming a downward flow parallel to the gravitational direction.

The second instability type can occur in the upper right quadrant, $0 < z < z_{crit}$, if $\frac{\partial \Delta c}{\partial z} > \partial \Delta c / \partial z \mid_{Ra^*=0} \geq 0$. It bears a certain similarity to the Rosensweig instability in a ferrofluid.[35] Due to its high initial susceptibility, even small magnetic fields are sufficient to lift the ferrofluid against gravity and /or to form characteristic spikes at their interface. Keeping in mind that the magnetic susceptibility of the $DyCl_3$ solution is smaller than that of a ferrofluid by a factor of more than 1000, the effects to be expected by the predicted susceptibility-driven instability will be significantly smaller.

7   Summary and conclusions

A dedicated experimental setup was developed to understand why previous experiments in rare earth solutions show a robust enrichment of paramagnetic ions in a magnetic field gradient contrary, to the expected delocalization by Brownian motion. The key element is the adjustment of an evaporative flux at the free surface of the $DyCl_3$ solution to prove that evaporation triggers this magnetic separation process.

Evaporation gives rise to fluxes of both heat and water molecules across the interface. Therefore, the resulting change in the refractive index of the $DyCl_3$ solution is affected by both the concentration and the temperature. To discriminate between the two contributions

1
2
3
4
5
6
7
8
9
10
11
12
13
14
15
16
17
18
19
20
21
22
23
24
25
26
27
28
29
30
31
32
33
34
35
36
37
38
39
40
41
42
43
44
45
46
47
48
49
50
51
52
53
54
55
56
57
58
59
60

in our Mach-Zehnder interferometry approach, a new two-step compensation algorithm was developed and applied together with numerical simulations of the concentration and temperature fields. By these means, we could clearly show that more than 90% of the refractive index increase in the boundary layer at the free surface most exposed to the field gradient is caused by the increase in the Dy(III) concentration. The close similarity of the present results to those obtained in seemingly closed cells furthermore conclusively proves the initial hypothesis that evaporation is the supporting process for the magnetic separation of RE ions.

To understand the underlying mechanism, we started out by analyzing the hydrostatics of the solution. We have shown that the unbalanced radial component of the field gradient force is responsible for shaping the evaporation-driven concentration boundary layer into the observed concave shape. Generally, the evaporation-driven concentration boundary layer is hydrodynamically unstable, because it is heavier than the underlying bulk fluid. It is the field gradient force, acting in the opposite direction to gravity, which suppresses the resulting Rayleigh-Taylor instability. We show that the gravitational force acting on the boundary layer, expressed in a non-dimensional manner by the Rayleigh number, is drastically diminished by the approximately five times larger magnetic field gradient force. As a result, the supercritical value of the Rayleigh number is reduced to a subcritical one at which the Rayleigh-Taylor instability cannot set in. This is the origin of the observed levitation of the Dy(III) boundary layer in the magnetic field gradient.

We next considered the competition between a change in the gravitational force and a change in the vertical magnetic field gradient force given a local concentration gradient. A conservatively approximated stability criterion is calculated using a resulting Rayleigh number equivalent to 0. Thus, $\partial \Delta c / \partial z \mid_{Ra^*=0}$ as a function on the $f_{m,z}$ shows a singularity at $z = z_{crit} \approx 3$ mm. Both lines, $\partial \Delta c / \partial z = 0$ and $z = z_{crit}$, divide the stability behavior of the system into two regions of instability and two regions of stability, see Fig. 11. According to this stability diagram, the evaporation-driven enrichment layer is found above $z > z_{crit}$,

28

i.e. in the zone where $f_{m,z}$ greatly dominates f_g and is therefore unconditionally stable in the present magnetic field. As a side product, a new susceptibility-driven instability is predicted provided $\partial\Delta c/\partial z > 0$ and $z < z_{crit}$, which should lead the solution to flow upwards.

Beside answering the important question of what mechanism underlies the observed magnetic separation of rare earth ions, the present study points to a series of issues in this process which have neither been addressed nor fully understood. As discussed above, a microconvection has to be responsible for the reshaping of the originally planar evaporation-driven boundary layer. There is a lack of experimental insights into this type of convection. As a consequence, also a more detailed stability analysis of the linearized Navier-Stokes equation [30] is desirable for a better understanding. This also holds for the predicted susceptibility-gradient-driven instability.

Acknowledgement

References

(1) Oberteuffer, J. Magnetic separation: A review of principles, devices, and applications. IEEE T. Magn. **1974**, 10, 223–238.

(2) Svoboda, J. Magnetic techniques for the treatment of materials; Kluwer Academic Publisher, 2004.

(3) Pamme, N.; Wilhelm, C. Continuous sorting of magnetic cells via on-chip free-flow magnetophoresis. Lab Chip **2006**, 6, 974–980.

(4) Franzreb, M.; Siemann-Herzberg, M.; Hobley, T. J.; Thomas, O. R. Protein purification using magnetic adsorbent particles. Appl. Microbiol. Biotechnol. **2006**, 70, 505–516.

(5) Bromberg, L.; Chang, E. P.; Alvarez-Lorenzo, C.; Magarinos, B.; Concheiro, A.; Hatton, T. A. Binding of functionalized paramagnetic nanoparticles to bacterial lipopolysaccharides and DNA. Langmuir **2010**, 26, 8829–8835.

(6) Uhlemann, M.; Tschulik, K.; Gebert, A.; Mutschke, G.; Fröhlich, J.; Bund, A.; Yang, X.; Eckert, K. Structured electrodeposition in magnetic gradient fields. Eur. Phys. J. Spec. Top. **2013**, 220, 287–302.

(7) Monzon, L. M.; Coey, J. Magnetic fields in electrochemistry: The Kelvin force. A mini-review. Electrochem. Commun. **2014**, 42, 42–45.

(8) Leventis, N.; Gao, X. Magnetohydrodynamic Electrochemistry in the Field of Nd- Fe- B Magnets. Theory, Experiment, and Application in Self-Powered Flow Delivery Systems. Anal. Chem. **2001**, 73, 3981–3992.

(9) Mutschke, G.; Tschulik, K.; Weier, T.; Uhlemann, M.; Bund, A.; Fröhlich, J. On the action of magnetic gradient forces in micro-structured copper deposition. Electrochim. Acta **2010**, 55, 9060–9066.

(10) Ngamchuea, K.; Tschulik, K.; Compton, R. G. Magnetic control: Switchable ultrahigh magnetic gradients at Fe3O4 nanoparticles to enhance solution-phase mass transport. Nano Res. **2015**, 8, 3293–3306.

(11) Dunne, P.; Coey, J. Patterning metallic electrodeposits with magnet arrays. Phys. Rev. B **2012**, 85, 224411.

(12) Tschulik, K.; Cierpka, C.; Mutschke, G.; Gebert, A.; Schultz, L.; Uhlemann, M. Clarifying the mechanism of reverse structuring during electrodeposition in magnetic gradient fields. Anal. Chem. **2012**, 84, 2328–2334.

(13) Yang, X.; Tschulik, K.; Uhlemann, M.; Odenbach, S.; Eckert, K. Enrichment of para-
magnetic ions from homogeneous solutions in inhomogeneous magnetic fields. J. Phys.
Chem. Lett. **2012**, 3, 3559–3564.

(14) Gorobets, O. Y.; Gorobets, Y. I.; Bondar, I.; Legenkiy, Y. A. Quasi-stationary hete-
rogeneous states of electrolyte at electrodeposition and etching process in a gradient
magnetic field of a magnetized ferromagnetic ball. J. Magn. Magn. Mater. **2013**, 330,
76–80.

(15) Yang, X.; Tschulik, K.; Uhlemann, M.; Odenbach, S.; Eckert, K. Magnetic Separation
of Paramagnetic Ions From Initially Homogeneous Solutions. IEEE T. Magn. **2014**, 50,
4600804.

(16) Pulko, B.; Yang, X.; Lei, Z.; Odenbach, S.; Eckert, K. Magnetic separation of Dy (III)
ions from homogeneous aqueous solutions. Appl. Phys. Lett. **2014**, 105, 232407.

(17) Udagawa, C.; Maeda, A.; Katsuki, A.; Maki, S.; Morimoto, S.; Tanimoto, Y. Magnetic
Field Effects on Copper Metal Deposition from Copper Sulfate Aqueous Solution. J.
Phys. Chem. B **2014**, 118, 4889–4894.

(18) Gorobets, O. Y.; Gorobets, Y. I.; Rospotniuk, V. Magnetophoretic potential at the mo-
vement of cluster products of electrochemical reactions in an inhomogeneous magnetic
field. J. Appl. Phys. **2015**, 118, 073902.

(19) Jiang, X.; Qiao, J.; Lo, I. M.; Wang, L.; Guan, X.; Lu, Z.; Zhou, G.; Xu, C. Enhanced
paramagnetic Cu 2+ ions removal by coupling a weak magnetic field with zero valent
iron. J. Hazard. Mater. **2015**, 283, 880–887.

(20) Kołczyk, K.; Wojnicki, M.; Kutyła, D.; Kowalik, R.; Żabiński, P.; Cristofolini, A. Se-
paration of Ho3+ in Static Magnetic Field. Arch. Metall. Mater **2016**, 61, 1919–1924.

(21) Franczak, A.; Binnemans, K.; Fransaer, J. Magnetomigration of rare-earth ions in inhomogeneous magnetic fields. Phys. Chem. Chem. Phys. **2016**,

(22) Binnemans, K.; Jones, P. T.; Blanpain, B.; Van Gerven, T.; Pontikes, Y. Towards zerowaste valorisation of rare-earth-containing industrial process residues: a critical review. J. Clean. Prod. **2015**, 99, 17–38.

(23) Binnemans, K.; Jones, P. T.; Blanpain, B.; Van Gerven, T.; Yang, Y.; Walton, A.; Buchert, M. Recycling of rare earths: a critical review. J. Clean. Prod. **2013**, 51, 1–22.

(24) Gorobets, O. Y.; Gorobets, Y. I.; Rospotniuk, V.; Kyba, A.; Legenkiy, Y. A. Liquid-liquid phase separation occurring under the influence of inhomogeneous magnetic field in the process of the metal deposition and etching of the magnetized ferromagnetic ball. J. Solid State Electrochem. **2015**, 19, 3001–3012.

(25) Baes, C. F.; Mesmer, R. E. Hydrolysis of cations; Wiley, 1976.

(26) Lei, Z.; Haberstroh, C.; Odenbach, S.; Eckert, K. Heat transfer enhancement in magnetic cooling by means of magnetohydrodynamic convection. Int. J. Refrig. **2016**, 62, 166–176.

(27) Lei, Z.; Yang, X.; Haberstroh, C.; Pulko, B.; Odenbach, S.; Eckert, K. Space-and time-resolved interferometric measurements of the thermal boundary layer at a periodically magnetized gadolinium plate. Int. J. Refrig. **2015**, 56, 246–255.

(28) Coey, J. M. D.; Aogaki, R.; Byrne, F.; Stamenov, P. Magnetic stabilization and vorticity in submillimeter paramagnetic liquid tubes. Proc. Natl. Acad. Sci. U.S.A. **2009**, 106, 8811–8817.

(29) Mutschke, G.; Tschulik, K.; Uhlemann, M.; Bund, A.; Fröhlich, J. Comment on Şmagnetic structuring of electrodepositsŤ. Phys. Rev. Lett. **2012**, 109, 229401.

(30) Chandrasekhar, S. Hydrodynamic and hydromagnetic stability; Courier Corporation, 2013.

(31) Finlayson, B. Convective instability of ferromagnetic fluids. J. Fluid Mech. **1970**, 40, 753–767.

(32) Schwab, L. Thermal convection in ferrofluids under a free surface. J. Magn. Magn. Mater. **1990**, 85, 199–202.

(33) Engler, H.; Odenbach, S. Parametric modulation of thermomagnetic convection in magnetic fluids. J. Phys.: Condens. Matter **2008**, 20, 204135.

(34) Lange, A.; Odenbach, S. Patterns of thermomagnetic convection in magnetic fluids subjected to spatially modulated magnetic fields. Phys. Rev. E **2011**, 83, 066305.

(35) Cowley, M.; Rosensweig, R. E. The interfacial stability of a ferromagnetic fluid. J. Fluid Mech. **1967**, 30, 671–688.
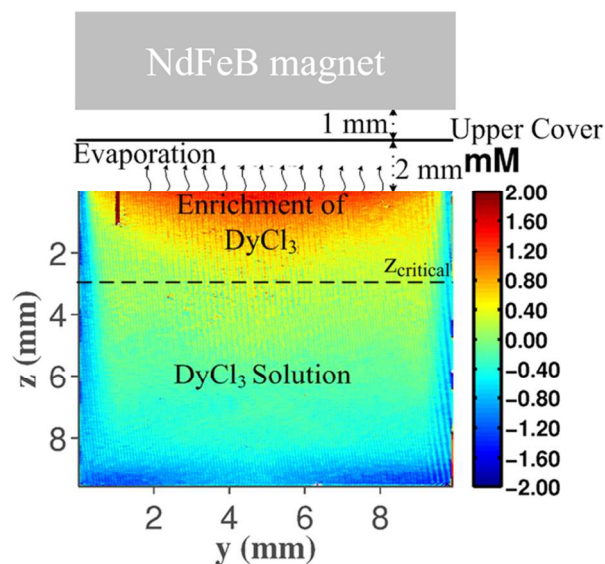
TOC: Enrichment of paramagnetic dysprosium ions in an initially homogenous solution when exposed to weak evaporation and a magnetic field gradient force

338x190mm (96 x 96 DPI)